

Quantification of red soil macropores affected by slope erosion and sediment using computed tomography

Si-Yi Zhang ^{1,2}, Bin He ^{1,2*}, Yan Sun ^{1,2}, Fan-Ling Kong ^{1,2}, Wan-Yi Huang ^{1,2}

¹ National-Regional Joint Engineering Research Center for Soil Pollution Control and Remediation in South China, Guangdong Key Laboratory of Integrated Agro-environmental Pollution Control and Management, Institute of Eco-environmental and Soil Sciences, Guangdong Academy of Sciences, Guangzhou 510650, China

² Guangdong-Hong Kong-Macao Joint Laboratory for Environmental Pollution and Control, Guangzhou 510650, China

* Correspondence: bhe@soil.gd.cn

Quantification of red soil macropores affected by slope erosion and sediment using computed tomography

Soil structure mechanism of collapsing gullies: Soil macropores, topography, water erosion and mass erosion

Abstract:

Purpose Soil structures are the main course of the formation and development of collapsing gullies, which are the most severe type of erosion in south China. However, few studies have focused on the relationship between soil macropores, soil erosion, and local topography. This study aimed to quantify and compare soil properties and macropore characteristics in the collapsing gully region, and explore their influences on the formation and development of the associated erosion.

Materials and methods Soil core columns at different positions of a typical collapsing gully were excavated, and then scanned to analyze soil macropores. Moreover, soil properties and saturated hydraulic conductivity were investigated in the laboratory and in the field, respectively.

Results and discussion The results indicated that the sand content increased from the ridge to the slope and the valley, while silt and clay contents decreased for the same catena. The mean weight diameter of aggregates was largest at the ridge and lowest at the valley. The infiltrate rates were highest at the valley and lowest at the slope. The valley had the greatest macroporosity ($1.09\pm0.33\%$), and the

highest number (5919 ± 703), volumes ($24.7 \pm 7.5 \text{ cm}^3$) and surface ($10.4 \pm 2.6 \text{ m}^2$) of macropores, as well as the highest connectivity (42.3), while the slope had the smallest macroporosity ($0.15 \pm 0.14\%$), and the smallest number (1189 ± 747), volumes ($3.4 \pm 3.2 \text{ cm}^3$) and surface ($1.7 \pm 1.4 \text{ m}^2$) of macropores. The mean pore volume of macropores larger than 1 mm^3 was largest at the ridge (16.8 ± 7.4), and smallest at the slope (10.6 ± 2.9). The number of macropores and their macroporosity mainly decreased with increasing depth, but were influenced by the soil macrofauna as well as the erosion and sediment processes. Macropores were mainly vertical, which is affected by the roots of plants and is conducive to the vertical infiltration of water. But, there were many horizontal macropores at the valley because of the sediment process. The equivalent pore diameter of macropores was mainly smaller than 2 mm (accounting for more than 76.3%), and the macropores larger than 5 mm were less than 1%.

Conclusions The macropore characteristics at different sites of the collapsing gullies affected the soil water infiltration and hydraulic conductivity, and further affected the processes of water erosion and mass erosion. The highest macroporosity at the valley would result in strong subsurface flow erosion and the loss of the base of collapsing wall. Macropores at the ridge would increase rain infiltration and promote soil collapsing. Few macropores and low infiltration abilities at the slope would strengthen the overland flow erosion. Thus, macropore characteristics had significant effects on both the formation and development of collapsing gullies.

Keywords: Soil macropores; computed tomography; erosion; sediment;
collapsing gully

1. Introduction

Collapsing gullies, also called “*Benggang*” by locals, are the most extensively eroded areas of the seven provinces of South China. Both mass erosion and water erosion occur synergistically on the weathering crust of granite, at a depth of dozens to hundreds of meters, in tropical and subtropical regions. This area contains more than 2.4×10^5 collapsing gullies, covering an area of 1.1×10^3 km² (Figure 1a), 45% of which are in Guangdong Province, which contains 74% of their total area (Liang *et al.*, 2009). More than 6.7×10^7 t yr⁻¹ of soil is lost because of these collapsing gullies, which damages farmland, houses, roads, bridges, reservoirs, and ponds, and causes economic losses of 3.2×10^9 USD, affecting 9.2×10^6 residents (Liang *et al.*, 2009). The occurring and developing mechanisms of collapsing gullies have rose many efforts of researchers, and soil macropore and soil water movement were thought to be important factors (Tao *et al.*, 2020).

Many factors influence both the spatial distribution and movement of soil water and other soil hydrological processes (Ghasemizade and Schirmer, 2013). The soil properties that particularly affect the soil hydrological process include soil structures, particle size distributions, porosities, soil layer characteristics,

oxidation-reduction characteristics, organic matter contents, soil water repellency, and the soil water content itself (Zhu *et al.*, 2012). Among these factors, the influence of macropores on soil water movement is of key importance (Lin *et al.*, 2010). Macropores allow rainfall to infiltrate into deeper soil layers, while impervious layers without macropores, such as caliche, prevent the continuous infiltration of water, thus leading to a higher soil water content above the caliche (Zhang *et al.*, 2012; Li *et al.*, 2013; Hu *et al.*, 2018). The macropore structures of soil in different slope positions differ because of the different characteristics of soil aggregates, gravel contents, and plant roots. This results in differences in soil water conductivity and preferential flow characteristics (Holden, 2009; Zhang *et al.*, 2016; Mei *et al.*, 2018; Hu *et al.*, 2020a). However, the preferential flow forms different macropore structures because of erosion (Nguyen *et al.*, 2019).

The tropical and subtropical regions of South China are subject to a lot of storm, but the alternations between dry and wet are obvious. Water is the limiting factor of the ecosystem service function during the dry season and also the driving factor of collapses, landslides, debris flows, and other disasters during the rainy season (Liang *et al.*, 2014; Tang *et al.*, 2014). The granite weathering crust in the study area can be divided into a topsoil layer, red soil layer, sand layer, debris layer, and spherical weathering layer from the top to the bottom (Tao *et al.*, 2017). It has been reported that the infiltration capacity of the red soil layer, sand layer, and debris layer decrease sequentially from surface to the deeper soil layers (Duan *et al.*, 2018). The water holding capacity of the topsoil layer and the red

soil layer is stronger than those of the sand layer and the debris layer. The soil water content gradually increases from the top to the bottom within the topsoil layer. However, the soil water content of the red soil layer to the debris layer gradually decreases. The farther away from the collapsing wall the site is, the higher its soil water content will be (Yusong *et al.*, 2015; Ni, 2016). The preferential flow varies by slope positions and soil layers (Tao *et al.*, 2017). There are more preferential flows at the red soil layer than at the sandy soil layer and the clastic layer (Zhao, 2016), which are affected by soil properties, precipitation characteristics, and the initial water content (Duan *et al.*, 2016). At present, studies of soil hydrology of collapsing gullies focus mostly on the characteristics and processes of hydrology, or on the characteristics of the physical and chemical properties of the soil. However, little research focuses on the comprehensive effects of geomorphology, vegetation, and soil properties, or their influence mechanism on soil hydrological process. Therefore, the influence of the soil macropore structure on soil hydrological processes, the mechanism of spatial distribution and transport of soil water, and their responses to future climate change are not fully clear.

The loose and deep granite crust forms the material basis of collapsing gullies, and both rainstorms and soil water accumulation are the main drivers of the development of collapsing gullies. Soil structural properties (e.g., soil particle compositions, bulk densities, and porosities) significantly vary in different layers of the deep granite crust (Liao *et al.*, 2018). This variation results in greatly

chinaXiv:202103.00125v1
122 differing soil mechanical characteristics in response to wetting (Xia *et al.*, 2018).
123 The increase of the soil water content after rainfall and infiltration will lead to an
124 increase of upper soil weight and a decrease of soil shear resistance, which in turn
125 results in the collapse of the granite soil wall (Zhang and Zhong, 1990). At the
126 same time, the decrease of the cohesion and internal friction angle of the granite
127 soil, as well as the increase of the pressure of the soil fissure flow when subjected
128 to water are the main causes of the granite soil wall collapse (Li, 1992).
129 Preferential flow along soil macropores is considered to be an important reason
130 for the spatial-temporal variation of the soil water content and soil fissure water
131 movement (Hencher and Beven, 2010).

132 Therefore, it is of great practical importance to study the soil macropores
133 of granite red soil, which will aid investigations of the hydrogeological process
134 toward a better understanding of the occurrence and development law of
135 collapsing gullies. This study also helps to effectively prevent, control, and
136 restore erosion-related damage in these regions.

138 2. Materials and Methods

139 2.1. Study sites

140 The soil cores were sampled at a collapsing gully at Huacheng Town
141 (24°04'N, 115°38'E), north of Wuhua County, Guangdong Province, China
142 (Figure 1). Collapsing gullies are often close to residential and agricultural

regions, and the often devastating soil erosion and mud sand flow events (Zhang and Liu, 2014) increase the risk for houses, roads, and farmlands (Figure 1b). Wuhua County is a representative subtropical monsoon region with a mean annual air temperature of 21.3 °C, and a mean annual precipitation of 1507.2 mm (Zhang *et al.*, 2020). The soil parent material is biotite granite and the weathering crusts are very deep, often exceeding 200 m. The soil is barren sandy loam with only 1.71 g kg⁻¹ of soil organic carbon (Zhang *et al.*, 2020). The vegetation is secondary with a coverage varying from 20% to 80% under different topographic and erosion conditions (Figure 1b). *Pinus massoniana* is the dominant constructive species, while *Dicranopteris dichotoma*, *Rhodomyrtus tomentosa*, *Miscanthus floridulus*, and *Baechea frutescens* form the main undergrowth (Zhang *et al.*, 2020). Three sites along a slope near a *Benggang*, the ridge site, slope site, and the valley site (Figure 1b), were chosen and a total of nine undisturbed soil cores were collected in three duplicates per site. The ridge and slope sites were covered by sparse *P. massoniana* with rare undergrowth vegetation, whereas, the valley site was mainly covered by *Phyllostachys edulis* with dense *D. dichotoma* and *Nephrolepis auriculata* as undergrowth.

<Figure 1>

2.2 Analysis of basic soil properties

For each site, three replicated soil samples were collected and soil properties were analyzed. Soils were air-dried at room temperature before sieving to 2 mm to analyze the soil particle size distribution with the pipette method (Gee

and Bauder, 1986). The aggregate size distribution was measured by separating different aggregates via wet sieving following a previously published method (Dong, 1997). First, field-moist soil samples were carefully passed through an 8-mm sieve (without breaking the soil structure) and then air-dried. Then, about 50 g of air-dried soil for each replicate was wet-sieved through a series of four sieves, which separated the samples into five different aggregate size fractions: >2000 μm large macroaggregates, 1000-2000 μm middle macroaggregates, 500-1000 μm small macroaggregates, 250-500 μm tiny macroaggregates, and 106-250 μm microaggregates. The four sieves were stacked so that the largest was at the top and the smallest at the bottom, and the soil sample was put into the top 2-mm sieve. Before wet-sieving, the soil samples were immersed in water on the top sieve for 5 min to break down aggregates via slaking pressure. Sieving was controlled by an Aggregate Analyzer (QT-WSI021, Qudaotech, Shanghai, China) with an up and down movement frequency of 30 times per min for a sieving period of 2 min. After sieving, each sieve was backwashed and the fraction that remained on the top of the sieve was collected, oven-dried at 105 °C, and weighed. The mean weight diameter (MWD) was computed as the sum of the oven-dried mass fraction of the soil remaining in each sieve after sieving, multiplied by the mean diameter of adjacent meshes (Le Bissonnais, 1996).

2.3 Field-saturated soil hydraulic conductivity measurements by DualHead Infiltrimeters

The field-saturated soil hydraulic conductivity (K_{fs}) was measured using a DualHead Infiltrimeter (Decagon Devices, Pullman, WA, USA) following an optimized method of Zhang *et al.* (2019). Before data collection, grass and vegetative litters were carefully removed and the surface soil temperature and water temperature were measured using ECH2O 5TE sensors (Meter Group, Pullman, WA, USA). An insertion ring with a depth of 5 cm and a radius of 7.5 cm was gently driven into the soil to ensure good contact with the soil and minimize disturbance. It was ensured that the ring was level in all orthogonal directions. K_{fs} was measured using a single cycle with 35 min holding time at each pressure head of 10 and 15 cm after 15 min of soaking. Only measurements without leakage and with coefficients of variation of the pressure head and water level below 15% were assumed to be reliable and used for further analyses. All K_{fs} values were viscosity-corrected to a standard temperature of 25 °C before comparison among different sites. This correction prevented the influence of changes in water effluent viscosity at different temperatures according to a previously described method (Zhang *et al.*, 2019).

2.4 Soil core samples

Polyvinyl chloride (PVC) cylinders with 5-mm wall thickness, 10-cm diameter, and 50-cm length were used to house intact soil. After a plot had been selected, the aboveground grass (if it existed) was clipped to ground level, and

the litter was removed to expose bare soil before soil sampling. The PVC cylinder was pushed into the soil using the instruments shown in Figure 2. Firstly, the ground spears (8) were revolved into the ground, and the support system (7, 6) was set up. An air-bubble level (9) was affixed on the top of the iron roof plate (6) to ensure that it was level. A steel tube (1) under the roof was used to house a PVC cylinder (4) with a window (2) on the upper side. The internal diameter of the steel tube (1) was only marginally larger than the external diameter of the PVC cylinder to limit its shifting. A steel cap was affixed on the top of the PVC cylinder. Then, a vertical hydraulic jack (3) was inserted between the roof (6) and the steel cap through the window (2) of the steel tube (1). The PVC cylinder (4) was pressed into the soil by driving the hydraulic jack (3) as the roof (6) was fixed by the struts (7) and the ground spears (8). As the hydraulic jack (3) reached its maximum lifting limit, it was taken out and reset. A log (5) with the same diameter of the PVC cylinder (4) and a height below the maximum lifting limit of the hydraulic jack (3) was put on the steel cap. The hydraulic jack (3) was inserted into the window (2) and driven again. These operations were repeated until the whole PVC cylinder (4) had penetrated the soil. To reduce the resistance of the soil layer, the roots of plants were cut, and to avoid damage from gravel, a steel ring knife (10) was installed at the bottom of the PVC cylinder. The inner diameter of the front blade of this steel ring knife is identical to the inner diameter of the PVC cylinder. The inside of the upper end of the ring knife featured a groove, whose inner diameter equals the outer diameter of the PVC cylinder (4).

There were also two small vertical windows at the bottom of the steel tube (1) for observing whether the PVC cylinder (4) had been completely pressed into the soil. This instrument can smoothly and vertically push the PVC cylinder into the soil without shock and rotation and can thus obtain the soil core with minimal disturbance. After the procedure, the PVC cylinder was dragged out, covered by a PVC cap at each end, and wrapped in a sponge to protect the soil from mechanical disturbances.

<Figure 2>

2.2. X-ray computed tomography scanning and image analysis

A Philips Medical Scanner (Royal Dutch Philips Electronics Ltd., Model: iCT 256, Amsterdam, Netherlands), a 256-slice spiral X-ray computed tomography (CT), was used to scan the obtained soil cores. The energy level was set to 140 kV and the X-ray tube current was 153 mA. The scanning was continuous with a slice thickness of 0.67 mm and a scan interval of 0.3 mm. After scanning and reorientation, an image sequence was produced with more than 1667 slices for each soil core, in a coronal view. Voxel Cone Tracing acquired 16-bit and 1024×1024 images with a voxel dimension of 0.122 mm × 0.122 mm × 0.3 mm (width × length × depth).

Images were analyzed using ImageJ software version 1.4.3.67 to examine the pore characteristics according to the following steps:

(1) Slices selection: To avoid voids and minimize disturbance caused by sampling, 100 slices (3 cm in depth) at the soil core head and 60 slices at the soil

core end were removed using the “Slice Remover” tool in ImageJ. Finally, 1500 slices (45 cm in depth) were selected for the following analyses.

(2) Region of interest selection: The “Region of Interest” tool was used to exclude voids near the core walls and to minimize the effects of beam hardening. A square area in the center of the soil core, with a diameter of 80 mm, was selected as region of interest and cropped for further analysis.

(3) Thresholding: The attenuation value of the obtained images ranged from -1024 to more than 3071. The intensity value of the water phantoms (mean = 0) was set as threshold value to differentiate air-filled spaces from other regions for image analysis. Values below the threshold were identified as air-filled pores, while values above the threshold were identified as non-pores (Feng *et al.*, 2003; Hu *et al.*, 2015). This threshold was also used by Udawatta *et al.* (2008) and performed well in the experiments for this study. Small PVC cylinders with known diameters were inserted into an undisturbed soil core and scanned, and this threshold analysis enabled interpretation of their pore sizes. After thresholding, the images were translated into binary images, where black areas represent the soil matrix and white areas represent macropores.

(4) Macropore analysis: After segmentation, the connectivity of soil macropores was estimated using the plugins “Purify” and “Connectivity” of ImageJ (in turn). The numbers of macropores, the macropore area, macropore perimeter, circularity, feret, and minimum feret of each slice were calculated using the “Analyze Particles” tool of ImageJ in 2D. A slice porosity was

calculated by the pore area of slices dividing the soil core area (5024 mm²). Previous studies classified pores with equivalent pore diameter (ϕ) > 0.1 mm as macropores (e.g. Harvey and Nuttle, 1995), and thus, the pores detected using CT (at a resolution of 0.122 mm × 0.122 mm) could all be defined as macropores. Other researchers reported that only pores with ϕ > 1 mm can be divided into macropores (Carey *et al.*, 2010), and therefore, the present study classified pores with ϕ > 1 mm as wide macropores to better distinguish them.

The numbers of macropore tubes, macropore volumes, and macropore surfaces were calculated with the plugin “3D objects counter”. These 3D pores were divided into wide macropores or macropores, depending on whether the volumes exceeded 1 mm³ or not, respectively. 3D visualization of soil macropore networks in the soil cores was reconstructed using the plugin “3D viewer”, and then, the skeleton of the 3D soil macropore networks was established using the plugin “Skeletonise 3D”. The numbers and lengths of both macropore tubes and their branches were analyzed using the plugin “Analyse skeleton”.

<Figure 3>

2.3. Statistical analyses

Differences among measured parameters within-group sites were analyzed using one-way analysis of variance (ANOVA) combined with Fisher’s protected least significant difference (LSD) test. All statistical analyses were conducted using SPSS software (version 19.0, IBM Inc., USA), applying a $p = 0.05$ level of confidence.

3. Results

3.1. Soil properties

Across the investigated catena, the soil properties varied greatly from the ridge to the valley (Table 1). The soils were clay loam, loam, and sandy loam at the ridge, slope, and valley, respectively. The sand contents increased from the ridge to the valley, while the clay contents followed the opposite trend, and silt contents were highest at the slope. The bulk densities at the ridge were insignificantly higher than at the slope, while bulk densities at both sites were significantly higher than at the valley floor for all depths. However, the differences of total porosity contrasted with the bulk density. The capillary porosities increased from the ridge to the valley but only showed significant differences between the ridge and the valley at 20-40 cm. No significant differences were found between non-capillary porosities of the 0-20 cm soil layers at different sites; however, at the 20-60 cm layer, the non-capillary porosities at the valley were significantly higher than both at the ridge and slope. The saturated soil moisture increased from the ridge to the valley; however, the field water capacity only showed a significant difference at the 20-40 cm layer. The aggregate weight percentages and MWD increased from the ridge to the valley. The K_{fs} of the ridge and slope were 135.7 ± 98.7 and 80.6 ± 56.1 mm h⁻¹, respectively. Ridge sites had higher K_{fs} than slope sites, but their differences were

not significant ($p = 0.449$). The K_{fs} at the valley could not be measured as it exceeded the maximum measurement range of the DualHead Infiltrrometer (1150 mm h⁻¹).

3.2. Visualization of macropore networks

Visualizations of soil macropore networks in soil columns are shown in Figure 4. Soils at the valley have the greatest macroporosity and more macropores than soils at the ridge; however, the soils at the slope have minimum macroporosity and macropores. At the ridge and slope, soil macropores are mainly distributed at the surface layer (0-15 cm), where they formed networks, while at deeper soil layers (>15 cm), soil macropores were fewer and isolated. Exceptionally, the Ridge #3 soil core showed many macropores at 15-35 cm depth, because this sample contained an ants nest at this depth. The soil columns of the valley showed high macroporosity at all depths (Valley #3). Sometimes, the macropores at the deeper layer (30-40 cm) showed higher numbers than those at the shallower layer (0-15 cm, Valley #2). The directions of soil macropores at the ridge and slope were mainly vertical with a few horizontal networks at the surface layer; however, the soil macropore directions of the valley were mainly horizontal, which differed from the other two sites.

3.3. CT-measured macropores and macroporosity of whole columns

The total number, volume, and surface of soil macropores, as well as the macroporosity at the valley, were significantly higher than those at the ridge and slope (Table 2). The wide macroporosities (volume > 1 mm³) were $3.3 \pm 1.9\%$,

1.4 \pm 1.4%, and 10.5 \pm 3.3% for soil columns at the ridge, slope, and valley, respectively, and the numbers of wide macropores (volume > 1 mm³) were 428 \pm 75, 266 \pm 188, and 1468 \pm 194, respectively. Although the numbers of wide macropores only supplied a small part of the total macropores detected by CT, the large macropore volumes and wide macroporosity accounted for the majority of the total macropore volume and macroporosity, respectively. The mean volume and mean surface of macropores did not show significant differences between different sites. The mean connectivity at different sites showed great differences (Table 2); however, the differences were insignificant since there were great variations among each site.

3.4. Spatial distribution of macropores

Large variations were found in the macropore number distribution along the depth for different sites (Figure 5). Although the trends were different in different replicates, the average trend of macropore numbers decreased with increasing soil depth. At the top 3 cm of the soil cores, the wide macropore numbers were 11.4, 10.4, and 27.5 at the ridge, slope, and valley, respectively. At the ridge, the average wide macropore number decreased to 7.4 at a depth of 3-6 cm and ranged between 4.8 and 3.7 at a depth of 33-45 cm. The average wide macropore number at the slope decreased to 3.8 at a depth of 6-9 cm and remained within the range between 1.9 and 3.2 at a depth of 27-45 cm. The wide macropore numbers at the valley were highest among the three sites with a maximum number of 27.7 at a depth of 3-6 cm. The numbers of total macropores also decreased

with increasing depth (Figure 5). The percentages of the wide macropore number to the total macropore number increased with soil depth at both the ridge and the valley.

Soil macroporosities differed greatly among the three investigated sites (Table 2), and also varied along depths based on the data of slices (Figure 6). Soil macroporosities mainly decreased with increasing soil depth except for Ridge #3 and Valley #2. At the top 3 cm of the analyzed soil cores, the mean macroporosities were 0.62%, 0.48%, and 2.04% for the ridge, slope, and valley, respectively. The macroporosities at the ridge remained above 0.50% over 12 cm depth and then became lower than their mean macroporosity of 0.34% except for the depths of 15-18 cm and 30-33 cm, where extended ant nests were accidentally sampled at Ridge #3. Ant nests are common in this region and it cannot be avoided that these are included in the sample. At the slope site, only macroporosities at soil layers above 9 cm depth exceeded 0.48%, and the macroporosities of the soil layers below this depth did not exceed 0.16%. The macroporosities in the valley were highest among the three sites for each layer, ranging from 0.27% to 1.33% at depths below 18 cm. The trends of the wide macroporosities were similar to those of the macroporosities (Figure 6) since wide macropores represent the majority of total macropore volume (Table 2).

3.5. Macropore size distribution

The macropore sizes (φ) mainly ranged between 0.1-1 and 1-2 mm, accounting for more than 44.0%, and 32.3%, respectively (Figure 7). $\varphi > 5$ mm

chinaXiv:202103.00125v1
381 were less than 1% of the total macropores at all three sites. At the slope site, the
382 percentage of 0.1-1 mm macropore was highest among the three sites, and the
383 percentages of the wide macropores larger than 2 mm were lowest. The
384 percentages of 1-4 mm wide macropores at the valley were highest among the
385 three sites, while the percentages of wide macropores >4 mm were highest at the
386 ridge.
387

388 4. Discussion

389 Macropore networks were distinctly different among different positions at
390 the collapsing gullies and different types of macropores were detected by CT.
391 Macropores formed by earthworms were highly continuous, relatively large, and
392 tubular (Luo *et al.*, 2010); however, earthworms were not found at the ridge and
393 slope since the soil was very barren with soil organic carbon levels as low as 1.71
394 g kg⁻¹ (Zhang *et al.*, 2020). However, a network of ant nests was unexpectedly
395 found in the middle of Ridge #3 (Figure 4). The ant network macropores were
396 characterized by several big chambers connected by tunnels, and these
397 characteristics were similar to those observed before Li *et al.* (2017), Li (2017).
398 Macropores formed by roots were highly continuous and round in shape, the size
399 of which generally decreased with depth. These macropores could be found in all
400 soil cores, especially within the top 10 cm, which is in accordance with the roots
401 that are mainly distributed within the topsoil layer. Smaller, more randomly

distributed, and less continuously macropores were likely inter-aggregate macropores, which formed by wetting and drying (Luo *et al.*, 2010; Hu *et al.*, 2015). These are also the main macropores at soil layers deeper than 20 cm at the ridge and slope sites. Another phenomenon is the presence of many horizontal macropores at the valley site. This is because plants generally have shallow roots and grow horizontally (e.g., bamboo) because of the high soil water level and the absence of water deficits in the valley.

In addition, the erosion and sediment process greatly affected the number, size, macroporosity, and continuity of soil macropores. Soil macropores at the slope were comparatively rare and small (Table 2), similar to previous findings of Zhang *et al.* (2016). Soil erosion was more intensive at the slope compared to the ridge (Sabzevari and Talebi, 2019), and the soil horizon A at the slope had eroded during observation. Soil horizon A usually has a higher porosity and more macropores than horizon B (Hu *et al.*, 2020b). The barren slope soil without horizon A also restricted the growth of plants and the *P. massoniana* growing there were aged and dwarfed without undergrowth, which further limited the macropore development. However, at the valley, the soil was deposited by floods from the slope, and many dead tree branches were buried in different layers, which then formed macropores after decomposition. Also, the sediment mainly consisted of sand with an abundance of inter-aggregate macropores.

Macropore characteristics altered at different sites, which affected the soil water movement and the processes of soil erosion and collapse. At the slope, few

macropores limited the infiltration capacity (Iversen *et al.*, 2012; Hu *et al.*, 2020a). Superimposing the flow from the upslope, the overland flow at the slope was strong and erosive. Severe erosion limited soil water because of few infiltrations, and soil barrenness caused by the loss of horizon A inhibited the establishment of plants. Thus, the interaction between the low number of soil macropores, low vegetation cover, and fierce overflow at the slope was mutually promoting. The development of slope erosion thus stretches into the collapsing gullies. This could be one of the evolutionary mechanisms of collapsing gullies after the destruction of the original vegetation. This agrees with previous literature, which proposed that collapsing gullies developed because of the loss of vegetation (Zhang and Zhong, 1990).

The ridge had more macropores, which were larger in size and volume, and the macroporosity was also higher than that of the slope. This was caused by the relatively weaker soil erosion and better vegetation conditions at the ridge compared with those at the slope. Activities of plant roots and soil macrofauna (e.g., ants) are advantageous for the formation of macropores. These conditions promote water infiltration at the ridge. According to former research, the soil water content is an important factor that promotes the development of an existing collapsing gully (Shi, 1984; Li, 1992). More rainfall infiltration decreases the shear resistance of the soil layer while it also adds to the weight of the soil column. These developments further increase the probability and risk of soil collapse and the development of a collapsing gully. Macropores decreased with increasing soil

depth, indicating that the infiltration ability decreases with increasing soil depth as Duan *et al.* (2018) reported. Thus, the soil water would remain at the topsoil layer, thus increasing the weight of the soil layer and decreasing the shear resistance of soil (Deng *et al.*, 2018).

The valley site was covered by sediment from the upslope and had an abundance of macropores. Consequently, infiltration would be large and the underground flow may be strong under these conditions. The high soil water content and subsurface flow increase the risk of subsurface flow erosion (Tebebu *et al.*, 2010). The sediment was sandy, containing only a little clay. It has been reported that alluvial sediment is very erosive when the vegetation cover is insufficient (Jiang *et al.*, 2020). As observed in the field, once the check dam was completely filled, the overland flow could easily erode the inside sediment and thus form a deep gully. Once the sediment was removed, the base of the collapsing wall would be lost, and the risk of collapse would increase without base support.

5. Conclusions

The purpose of this study was to quantify the macropore features of soil using CT at different sites of a region with collapsing gullies. The results yielded macropore information about the effects of soil erosion and sediments on the soil structure and clarified an aspect of their interaction. The ridge had more and larger

macropores than the slope, while the sediment at the valley had the most macropores. The numbers of macropore and their macroporosities mostly decreased with increasing soil depth. The equivalent pore diameter of macropores mainly remained below 2 mm. These characteristics differed according to the tomography position, soil erosion, plant cover, and soil macrofauna. The high macroporosities of the valley and ridge increase the risks of subsurface flow erosion and soil collapse, which would promote the development of collapsing gullies. The soil macropores at the slope were rare and infiltration abilities were comparatively small; thus, overland flow and slope erosion can be assumed to be strengthened. These effects contribute to the formation of collapsing gullies.

Acknowledgements

This work was supported by the National Natural Science Foundation of China (Grant Nos. NSFC 41977010, 41930865 and 41807143), the Guangdong Basic and Applied Basic Research Foundation (Grant Nos. 2019A1515010628 and 2018A030313696), the GDAS Special Project of Science and Technology Development, China (Grant Nos. 2020GDASYL-20200102013 and 2020GDASYL-20200301003), Guangdong Foundation for Program of Science and Technology Research (2019QN01L682, 2019B121205006, 2019B121201004).

487 **References**

- Carey SK, Quinton WL, Goeller NT. 2010. Field and laboratory estimates of pore size properties and hydraulic characteristics for subarctic organic soils. *Hydrological Processes* **21**(19): 2560-2571.
- Deng Y, Duan X, Ding S, Cai C, Chen J. 2018. Suction stress characteristics in granite red soils and their relationship with the collapsing gully in south China. *Catena* **171**: 505-522. DOI: <https://doi.org/10.1016/j.catena.2018.07.043>
- Dong M. 1997. Survey, observation and analysis of terrestrial biocommunities. Beijing: Standard Press of China. (In Chinese)
- Duan X, Deng Y, Tao Y, He Y, Lin L, Chen J. 2018. Variation in soil saturated hydraulic conductivity along the hillslope of collapsing granite gullies. *Hydrological Sciences Journal* **63**(5): 803-817. DOI: 10.1080/02626667.2018.1453610
- Duan X, Ni C, Chen J, Chen J. 2016. Study on the preferential flow of red soil erosion in granite slope collapse with high frequency monitoring of water content. *Journal of Soil and Water Conservation* **30**(5): 82-88. (In Chinese with English abstract)
- Feng J, Zhang J, Zhu A, Bi J. 2003. Soil Macropore Structure Characterized by X-Ray Computed Tomography. *Pedosphere* (4): 289-298.
- Gee GW, Bauder JW. 1986. Particle-size analysis. *Agronomy (USA)*.
- Ghasemizade M, Schirmer M. 2013. Subsurface flow contribution in the hydrological cycle: Lessons learned and challenges ahead-A review. *Environmental Earth Sciences* **69**(2): 707-718.
- Harvey JW, Nuttle WK. 1995. Fluxes of water and solute in a coastal wetland sediment. 2. Effect of macropores on solute exchange with surface water. *Journal of Hydrology* **164**(1): 109-125. DOI: [https://doi.org/10.1016/0022-1694\(94\)02562-P](https://doi.org/10.1016/0022-1694(94)02562-P)
- Hencher SR, Beven KJ. 2010. Preferential flow paths through soil and rock and their association with landslides. *Hydrological Processes* **24**(12): 1610-1630.
- Holden J. 2009. Topographic controls upon soil macropore flow. *Earth Surface Processes and Landforms* **34**(3): 345-351. DOI: 10.1002/esp.1726
- Hu X, Li X, Guo L, Liu Y, Wang P, Zhao Y, Cheng Y, Lyu Y, Liu L. 2018. Influence of shrub roots on soil macropores using X-ray computed tomography in a shrub-encroached grassland in Northern China. *Journal of Soils and Sediments*. DOI: 10.1007/s11368-018-2218-6
- Hu X, Li X, Li Z, Gao Z, Wu X, Wang P, Lyu Y, Liu L. 2020a. Linking 3-D soil macropores and root architecture to near saturated hydraulic conductivity of typical meadow soil types in the Qinghai Lake Watershed, northeastern Qinghai – Tibet Plateau. *Catena* **185**: 104287. DOI: 10.1016/j.catena.2019.104287
- Hu X, Li X, Li Z, Liu L. 2020b. 3-D soil macropore networks derived from X-ray tomography in an alpine meadow disturbed by plateau pikas in the Qinghai Lake watershed, north-eastern Qinghai-Tibetan Plateau. *Journal of Soils and Sediments*. DOI: 10.1007/s11368-019-02560-8
- Hu X, Li Z, Li X, Liu Y. 2015. Influence of shrub encroachment on CT-measured soil macropore characteristics in the Inner Mongolia grassland of northern China. *Soil and Tillage Research* **150**: 1-9. DOI: 10.1016/j.still.2014.12.019
- Iversen BV, Lamandé M, Torp SB, Greve MH, Heckrath G, de Jonge LW, Moldrup P, Jacobsen OH. 2012. Macropores and macropore transport: relating basic soil properties to macropore density and soil hydraulic properties. *Soil Science* **177**(9): 535-542. DOI: 10.1097/SS.0b013e31826dd155
- Jiang F, He K, Lin J, Li H, Zhan Z, Lin J, Ge H, Wang MK, Huang Y. 2020. A comparison of the effectiveness of the roots of two grass species in reducing soil erosion on alluvial fans in south-east China. *Hydrological Processes* **34**(1): 96-110. DOI: 10.1002/hyp.13575
- Le Bissonnais YL. 1996. Aggregate stability and assessment of soil crustability and erodibility: I. Theory and methodology. *European Journal of Soil Science* **47**(4): 425-437.
- Li S. 1992. Study on erosion law and control of slope disintegration in Guangdong province. *Journal of natural disasters* **1**(3): 68-74. (In Chinese with English abstract)
- Li T, Shao MA, Jia Y. 2017. Effects of activities of ants (*Camponotus japonicus*) on soil moisture cannot be neglected in the northern Loess Plateau. *Agriculture, Ecosystems & Environment* **239**: 182-187. DOI: <https://doi.org/10.1016/j.agee.2017.01.024>
- Li T. 2017. Characteristics of soil macropore on the loess plateau and their effects on soil water. Xi'an: Northwest Agriculture and Forest University. (In Chinese with English abstract)
- Li X, Zhang S, Peng H, Hu X, Ma Y. 2013. Soil water and temperature dynamics in shrub-encroached grasslands and climatic implications: Results from Inner Mongolia steppe ecosystem of north China. *Agricultural and Forest Meteorology* **171 – 172**: 20-30.

- Liang W, Hung F, Chan M, Lu T. 2014. Spatial structure of surface soil water content in a natural forested headwater catchment with a subtropical monsoon climate. *Journal of Hydrology* **516**: 210-221. DOI: 10.1016/j.jhydrol.2014.01.032
- Liang Y, Ning D, Pan X, Li D, Zhang B. 2009. Characteristics and management of Benggang in red soil region of southern China. *Soil and Water Conservation in China* (1): 31-34. (In Chinese with English abstract)
- Liao Y, Tang C, Yuan Z, Zhuo M, Huang B, Nie X, Xie Z, Li D. 2018. Research Progress on Benggang Erosion and Its Prevention Measure in Red Soil Region of Southern China. *Acta Pedologica Sinica* **55**(6): 1297-1312. (In Chinese with English abstract)
- Lin H, Flüßler H, Otten W, Vogel H. 2010. Soil architecture and preferential flow across scales. *Journal of Hydrology* **393**(1): 1-2. DOI: <https://doi.org/10.1016/j.jhydrol.2010.07.026>
- Luo L, Lin H, Li S. 2010. Quantification of 3-D soil macropore networks in different soil types and land uses using computed tomography. *Journal of Hydrology* **393**(1-2): 53-64. DOI: 10.1016/j.jhydrol.2010.03.031
- Mei X, Zhu Q, Ma L, Zhang D, Wang Y, Hao W. 2018. Effect of stand origin and slope position on infiltration pattern and preferential flow on a Loess hillslope. *Land Degradation & Development* **29**(5): 1353-1365. DOI: 10.1002/ldr.2928
- Nguyen CD, Benahmed N, Andò E, Sibille L, Philippe P. 2019. Experimental investigation of microstructural changes in soils eroded by suffusion using X-ray tomography. *Acta Geotechnica* **14**(3): 749-765. DOI: 10.1007/s11440-019-00787-w
- Ni C. 2016. Study on soil moisture distribution in a granitic Benggang hillslope. Wuhan: Huazhong Agriculture University. (In Chinese with English abstract)
- Sabzevari T, Talebi A. 2019. Effect of hillslope topography on soil erosion and sediment yield using USLE model. *Acta Geophysica* **67**(6): 1587-1597. DOI: 10.1007/s11600-019-00361-8
- Shi D. 1984. An analysis of the erosion of collapsing gullies in the tropics and subtropics of China. *Bulletin of soil and water conservation* (3): 32-37. (In Chinese with English abstract)
- Tang Y, Wen X, Sun X, Zhang X, Wang H. 2014. The limiting effect of deep soil water on evapotranspiration of a subtropical coniferous plantation subjected to seasonal drought. *Advances in Atmospheric Sciences* **31**(2): 385-395. DOI: 10.1007/s00376-013-2321-y
- Tao Y, He Y, Duan X, Zou Z, Lin L, Chen J. 2017. Preferential flows and soil moistures on a Benggang slope: Determined by the water and temperature co-monitoring. *Journal of Hydrology* **553**: 678-690. DOI: <https://doi.org/10.1016/j.jhydrol.2017.08.029>
- Tao Y, Zou Z, Guo L, He Y, Lin L, Lin H, Chen J. 2020. Linking soil macropores, subsurface flow and its hydrodynamic characteristics to the development of Benggang erosion. *Journal of Hydrology* **586**: 124829. DOI: 10.1016/j.jhydrol.2020.124829
- Tebebu TY, Abiy AZ, Zegeye AD, Dahlke HE, Easton ZM, Tilahun SA, Collick AS, Kidnau S, Moges S, Dadgari F, Steenhuis TS. 2010. Surface and subsurface flow effect on permanent gully formation and upland erosion near Lake Tana in the northern highlands of Ethiopia. *Hydrology and Earth System Sciences* **14**(11): 2207-2217. DOI: 10.5194/hess-14-2207-2010
- Udawatta RP, Anderson SH, Gantzer CJ, Garrett HE. 2008. Influence of Prairie Restoration on CT-Measured Soil Pore Characteristics. *Journal of Environment Quality* **37**(1): 219. DOI: 10.2134/jeq2007.0227
- Xia D, Zhao B, Liu D, Deng Y, Cheng H, Yan Y, Ding S, Cai C. 2018. Effect of soil moisture on soil disintegration characteristics of different weathering profiles of collapsing gully in the hilly granitic region, South China. *PLoS One* **13**(e020942712). DOI: 10.1371/journal.pone.0209427
- Yusong D, Shuwen D, Chenming L, Dong X, Xiaoming Z, Guoan LV. 2015. Soil Moisture Characteristics of Collapsing Gully Wall in Granite Area of Southeastern Hubei. *Journal of Soil and Water Conservation* **29**(4): 132-137. (In Chinese with English abstract) DOI: 10.13870/j.cnki.stbcbx.2015.04.025
- Zhang D, Liu X. 2014. Analysis of the grain size properties and flow body classes of the mud sand flow: An example of Liantanggang collapsing hill and gully in Wuhua County of Guangdong. *Advances in Earth Science* **29**(7): 810-818. (In Chinese with English abstract)
- Zhang S, Hopkins I, Guo L, Lin H. 2019. Dynamics of Infiltration Rate and Field-Saturated Soil Hydraulic Conductivity in a Wastewater-Irrigated Cropland. *Water* **11**(8): 1632. DOI: 10.3390/w11081632
- Zhang S, Li X, Peng H, Zhang Z. 2012. Infiltration pattern beneath shrub canopy and interspace grass patches in typical steppe ecosystems of Inner Mongolia, China. *Journal of Earth Environment* **6**(3): 1117-1125.
- Zhang S, Zhong C. 1990. The mechanism and types of the hillock collapsing forming in Guangdong province. *Bulletin of soil and water conservation* **10**(3): 8-16. (In Chinese with English abstract)
- Zhang S, Zhuo M, Xie Z, Yuan Z, Wang Y, Huang B, Liao Y, Li D, Wang Y. 2020. Effects of near soil surface components on soil erosion on steep granite red soil colluvial deposits. *Geoderma* **365**: 114203. DOI: 10.1016/j.geoderma.2020.114203
- Zhang Z, Lin L, Wang Y, Peng X. 2016. Temporal change in soil macropores measured using tension infiltrometer under different land uses and slope positions in subtropical China. *Journal of Soils and Sediments* **16**(3): 854-863. DOI: 10.1007/s11368-015-1295-z

603 Zhao X. 2016. Study on the migration of soil moisture and water infiltration characteristics of preferential flow.
604 Fuzhou: Fujian Agriculture and Forestry University. (In Chinese with English abstract)
605 Zhu Q, Liao K, Xu Y, Yang G, Wu S, Zhou S. 2012. Monitoring and prediction of soil moisture spatial-temporal
606 variations from a hydropedological perspective: a review. *Soil Research* **50**(8): 625-637. DOI:
607 10.1071/SR12228
608

609

610 Table 1 Soil properties at the ridge, slope, and valley of collapsing gully region. Values are average \pm standard deviation, based on three replicates.

Sites	Depth	Sand	Silt	Clay	Bulk density	Total porosity	Capillary porosity	Non-capillary porosity	Saturated soil moisture	Field water capacity	Aggregate weight percentage	MWD
	cm	g kg ⁻¹	g kg ⁻¹	g kg ⁻¹	g/cm ³	%	%	%	% (W/DW)	%(W/DW)	%(W/DW)	mm
Ridge	0-20	367.7 \pm 75.5a	312.3 \pm 19.8	320.0 \pm 57.4a	1.49 \pm 0.04a	40.48 \pm 1.48a	37.99 \pm 2.56a	1.65 \pm 0.06a	27.24 \pm 1.53a	21.11 \pm 1.98	28.13 \pm 7.44a	1.03 \pm 0.25a
	20-40				1.47 \pm 0.04a	41.96 \pm 2.19a	39.60 \pm 3.40a	1.40 \pm 0.25a	28.67 \pm 2.36a	22.78 \pm 3.15a	31.13 \pm 14.74a	0.87 \pm 0.2a
	40-60				1.47 \pm 0.03a	41.82 \pm 2.82a	39.27 \pm 4.14a	1.49 \pm 0.24a	28.45 \pm 2.12a	22.75 \pm 3.50	25.53 \pm 10.24a	0.74 \pm 0.1a
Slope	0-20	464.6 \pm 16.9ab	409.4 \pm 83.7	126.0 \pm 100.6b	1.31 \pm 0.11a	43.17 \pm 2.20a	41.39 \pm 2.2ab	1.79 \pm 0.28aA	33.07 \pm 2.44a	25.02 \pm 4.57	34.99 \pm 17.89a	1.12 \pm 0.18a
	20-40				1.41 \pm 0.04a	43.66 \pm 2.06a	42.11 \pm 2.03a	1.54 \pm 0.09aAB	30.98 \pm 2.19a	24.54 \pm 3.84a	37.82 \pm 12.25b	0.98 \pm 0.14b
	40-60				1.42 \pm 0.02a	43.38 \pm 1.41ab	41.96 \pm 1.44ab	1.42 \pm 0.06aB	30.65 \pm 1.42a	24.91 \pm 3.02	40.45 \pm 8.85b	1.01 \pm 0.1b
Valley	0-20	545.3 \pm 60.4b	335.8 \pm 44.8	118.9 \pm 15.7b	1.08 \pm 0.14b	49.46 \pm 6.13b	47.50 \pm 6.46b	1.95 \pm 0.36a	46.65 \pm 10.87b	29.94 \pm 10.3	65.15 \pm 27.63b	1.65 \pm 0.37b
	20-40				0.98 \pm 0.04b	51.55 \pm 0.94b	49.34 \pm 0.51b	2.22 \pm 0.61b	52.46 \pm 2.93b	32.76 \pm 3.92b	45.7 \pm 11.79bc	1.31 \pm 0.32c
	40-60				1.11 \pm 0.13b	46.72 \pm 3.03b	44.75 \pm 2.95b	1.97 \pm 0.18b	42.50 \pm 7.43b	21.74 \pm 2.68	47.73 \pm 17.95b	1.53 \pm 0.29c

611 MWD: mean weight diameter of aggregates; W: weight; DW: dry weight. At the same depths, sites with different lowercase
612 letters indicate significant differences ($p < 0.05$), while the same lowercase letter indicate no significant differences ($p > 0.05$).
613 At the same sites, Layers of different depth with different capital letters indicate significant differences ($p < 0.05$), while the
614 same capital letter indicate significant differences ($p > 0.05$).

616

617 Table 2 Characteristics of macropores of different stages of the slope. V is the volume of macropores.

Stages	Macropore number		Volume		Surface		Macroporosity		Mean macropore size	Mean surface	Connectivity
	Total	$V \geq 1 \text{ mm}^3$	Total cm^3	$V \geq 1 \text{ mm}^3$ cm^3	Total m^2	$V \geq 1 \text{ mm}^3$ m^2	Total %	$V \geq 1 \text{ mm}^3$ %	$V \geq 1 \text{ mm}^3$ mm^3	$V \geq 1 \text{ mm}^3$ mm^2	
Ridge mid-erosion	1828±324b	428±75b	7.8±4.4b	7.5±4.3b	2.9±1.2b	2.6±1.1b	0.34±0.19b	0.33±0.19b	16.8±7.4	58.8±18.5	15.1±25.6
Slope max-erosion	1189±747b	266±188b	3.4±3.2b	3.2±3.1b	1.7±1.4b	1.5±1.3b	0.15±0.14b	0.14±0.14b	10.6±2.9	51.8±8.6	5.9±8.9
Valley deposit	5919±703a	1468±194a	24.7±7.5a	23.7±7.5a	10.4±2.6a	9.2±2.6a	1.09±0.33a	1.05±0.33a	15.9±3.2	62.1±9.8	42.3±40.1

618

619 Figure captions:

620 Figure 1 (a) The location of soil core sampling sites in Guangdong Province, China, and
621 (b) their geomorphic and environment around. Shaded provinces in (a) represent
622 the main distribution areas of Benggang.

623 Figure 2 The instrument used to push the polyvinyl chloride cylinders into ground. 1 - steel
624 tube, 2 - window, 3 - lifting assembly (vertical hydraulic jack); 4 - sampling tube (PVC
625 cylinder); 5 - log plate; 6 - steel roof; 7 - struts; 8 - ground spear; 81 - ring; 82 - limit part; 83 -
626 crack; 84 - down warping part; 85 - up warping part; 9 - level; 10 - steel ring knife; 101 - front
627 blade; 102 - groove.

628 Figure 3 Procedures of image analysis in the study.

629 Figure 4 Three-dimensional visualization of soil macropore networks in the soil columns and
630 soil macroporosity along the soil depth at the ridge, slope, and valley. The number after ridge,
631 slope, or valley is the replicated column number.

632 Figure 5 The macropore numbers along the soil depth at (a) the ridge, (b) the slope, and (c) the
633 valley. The black, red, and green solid lines are the macropore numbers of three replicates with
634 the blue solid line being their mean for each 3 cm depth. The blue short dash lines are the
635 number of macropores with equivalent pore diameter > 1 mm.

636 Figure 6 Distribution of macroporosity along the soil column depth at the ridge, slope, and
637 valley.

638 Figure 7 The frequency of equivalent pore diameters of soil columns at different sites.

639

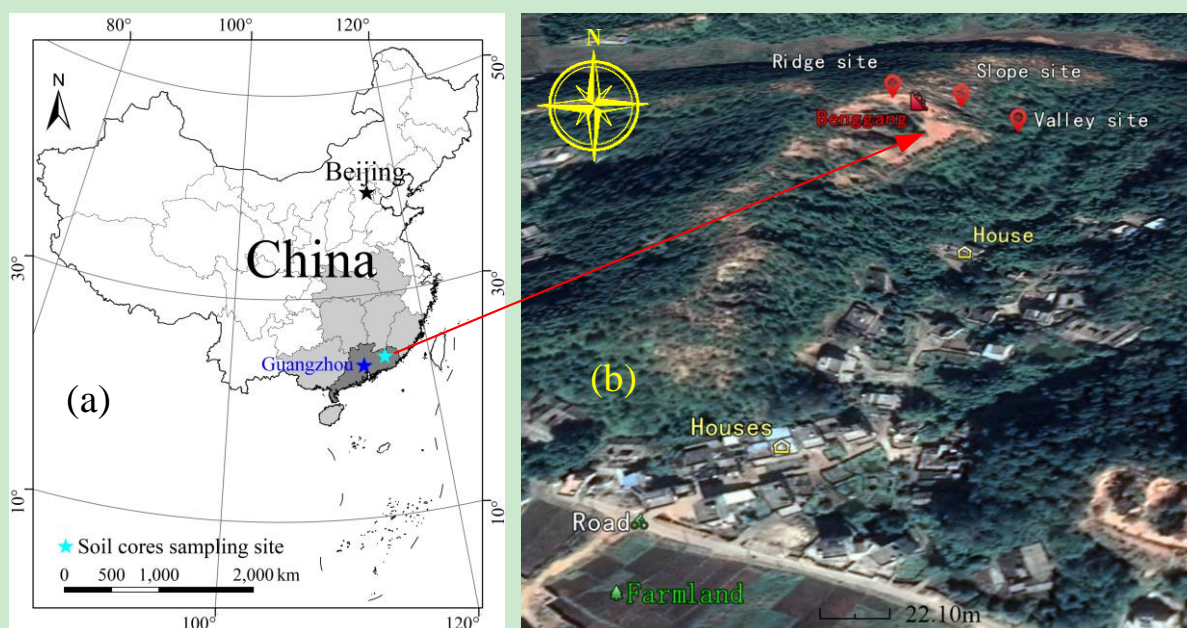


Figure 1 (a) The location of soil core sampling sites in Guangdong Province, China, and (b) their geomorphic and environment around. Shaded provinces in (a) represent the main distribution areas of *Benggang*.

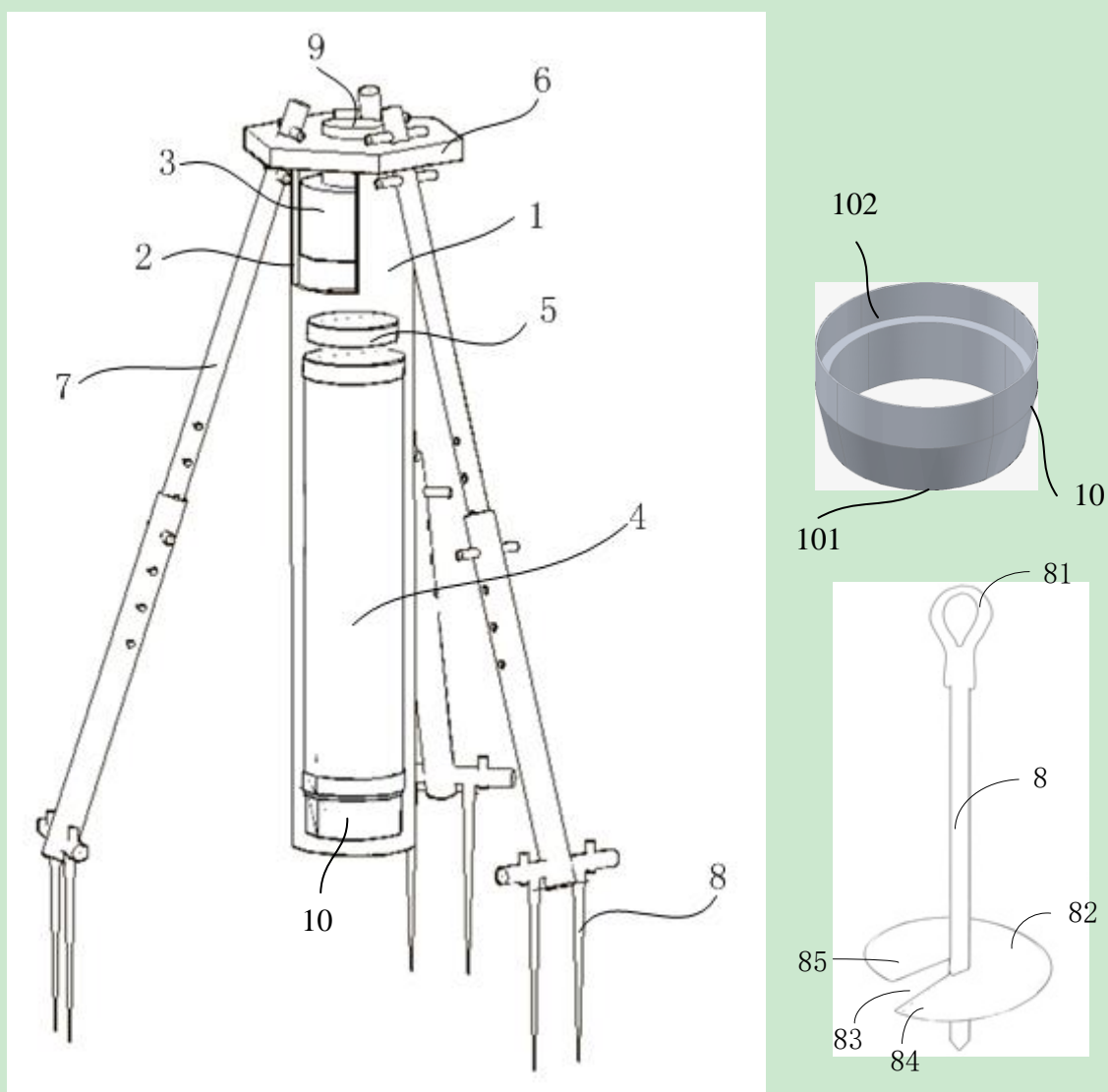


Figure 2 The instrument used to push the polyvinyl chloride cylinders into ground. 1 - steel tube, 2 - window, 3 - lifting assembly (vertical hydraulic jack); 4 - sampling tube (PVC cylinder); 5 - log plate; 6 - steel roof; 7 - struts; 8 - ground spear; 81 - ring; 82 - limit part; 83 - crack; 84 - down warping part; 85 - up warping part; 9 - level; 10 - steel ring knife; 101 - front blade; 102 - groove.

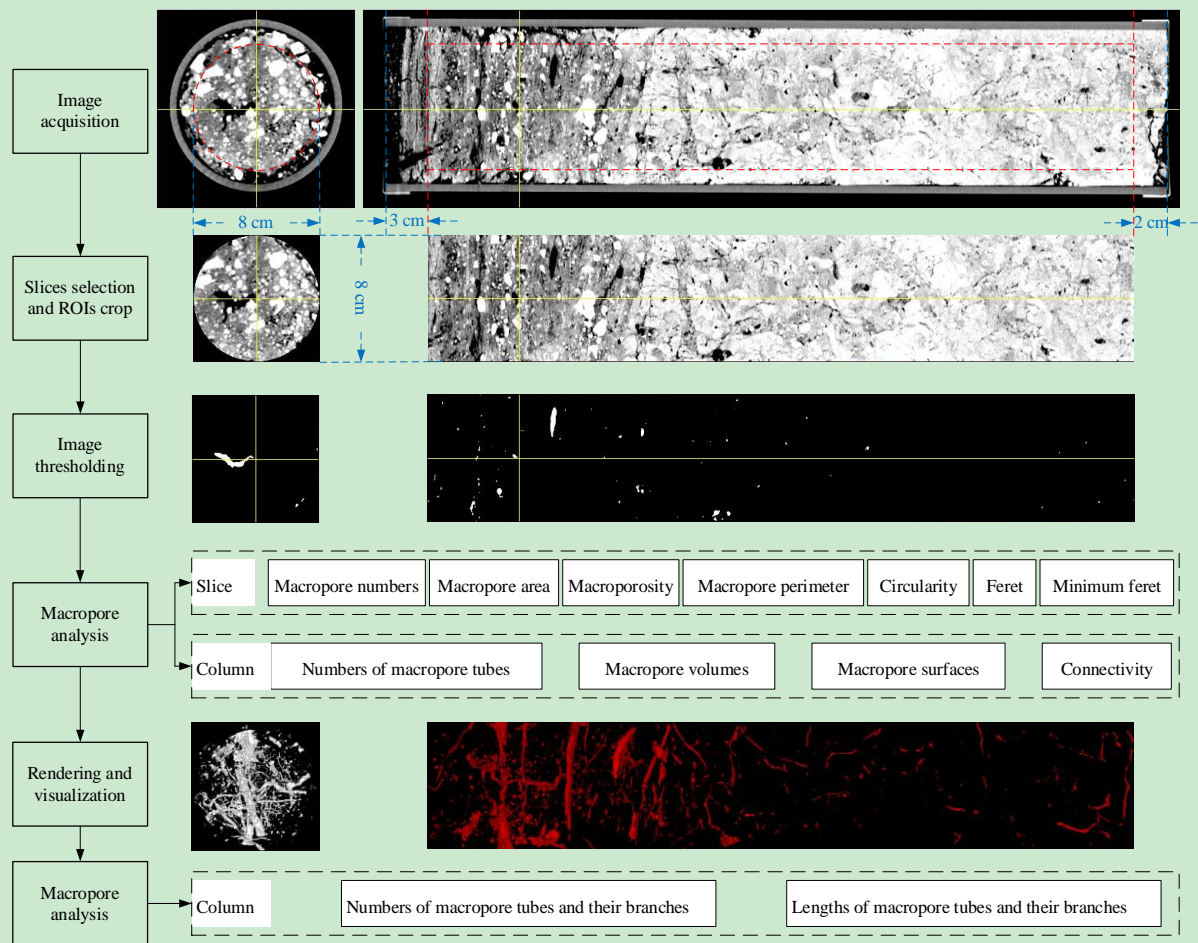
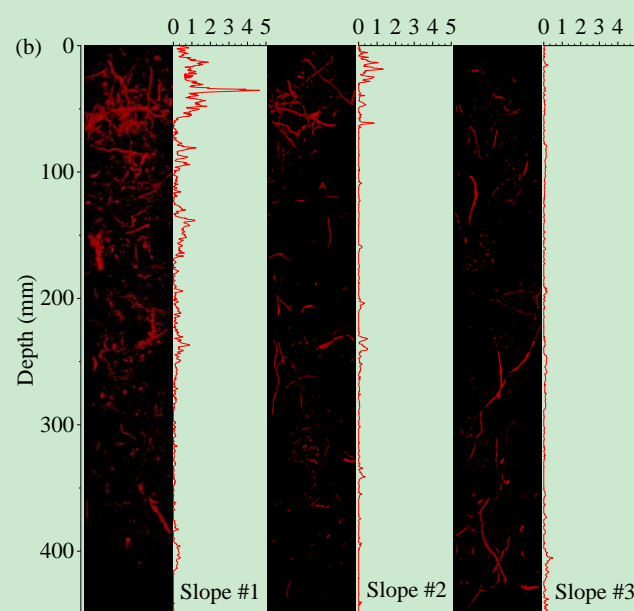
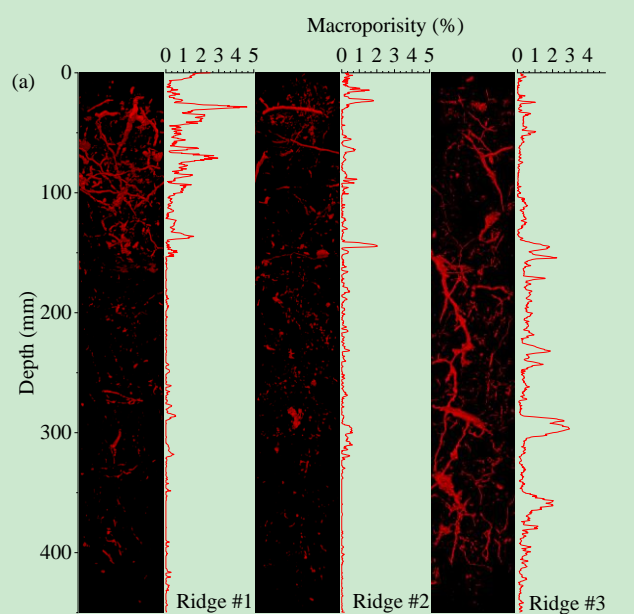


Figure 3 Procedures of image analysis in the study.



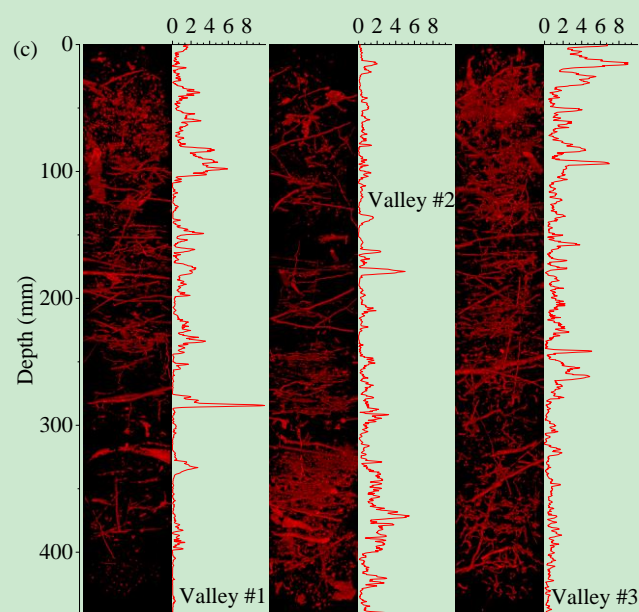


Figure 4 Three-dimensional visualization of soil macropore networks in the soil columns and soil macroporosity along the soil depth at the ridge, slope, and valley. The number after ridge, slope, or valley is the replicated column number.

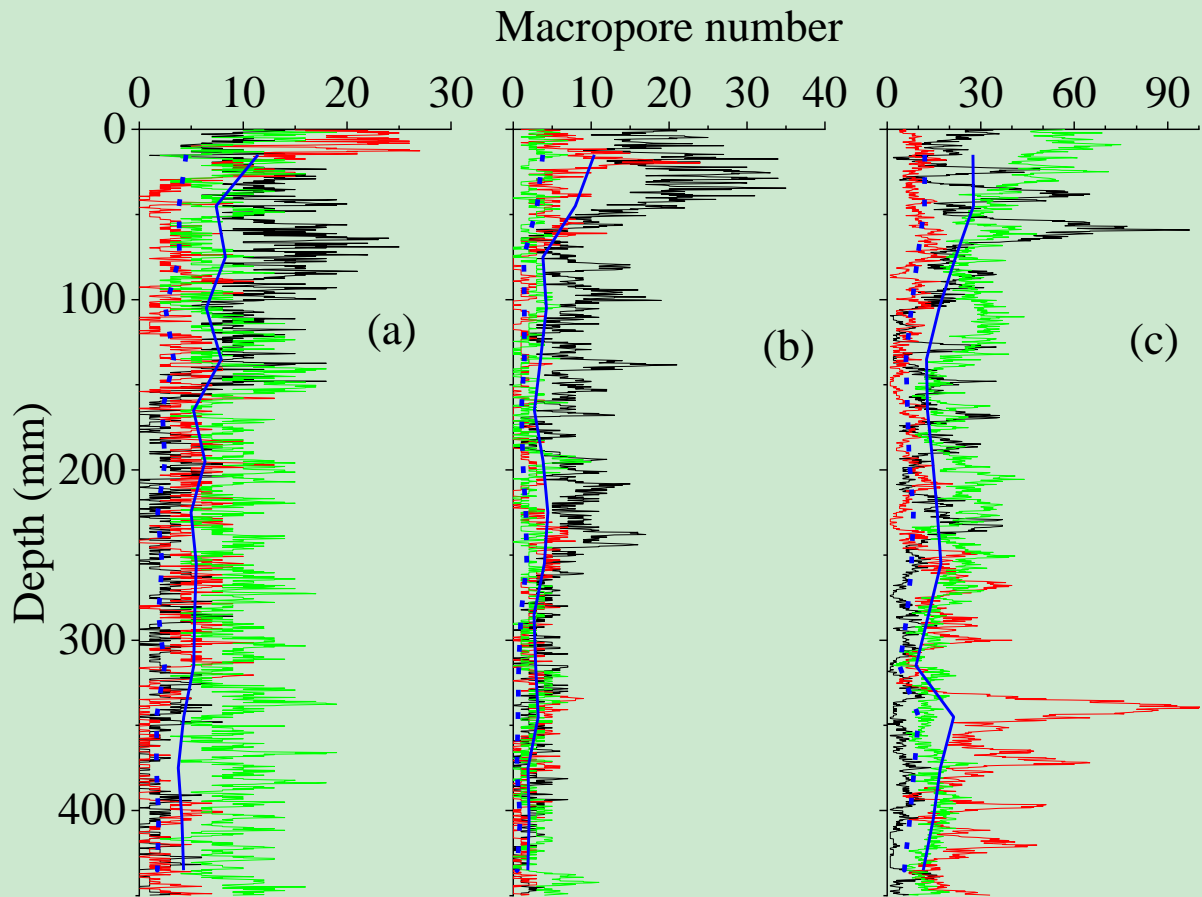


Figure 5 The macropore numbers along the soil depth at (a) the ridge, (b) the slope, and (c) the valley. The black, red, and green solid lines are the macropore numbers of three replicates with the blue solid line being their mean for each 3 cm depth. The blue short dash lines are the number of macropores with equivalent pore diameter > 1 mm.

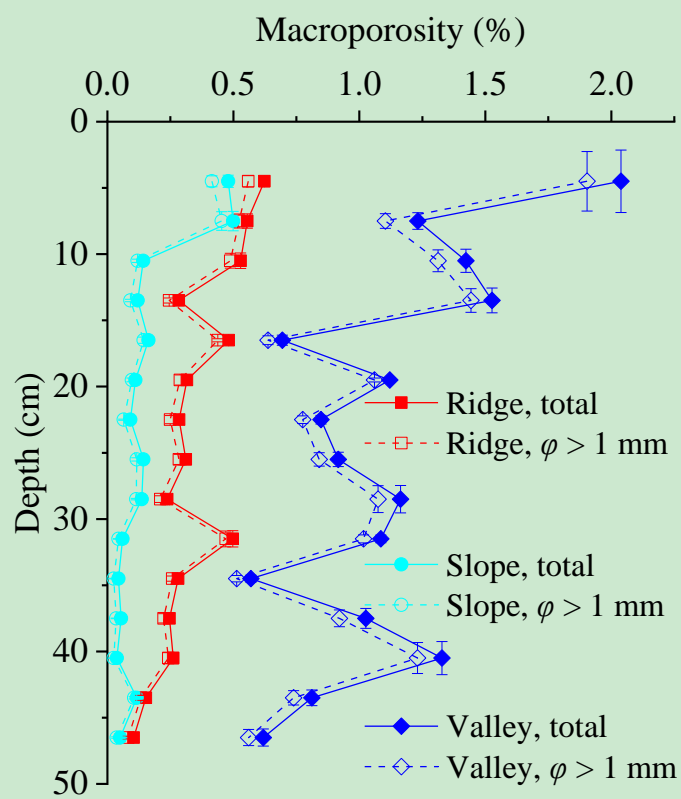


Figure 6 Distribution of macroporosity along the soil column depth at the ridge, slope, and valley. The ϕ is equivalent pore diameter.

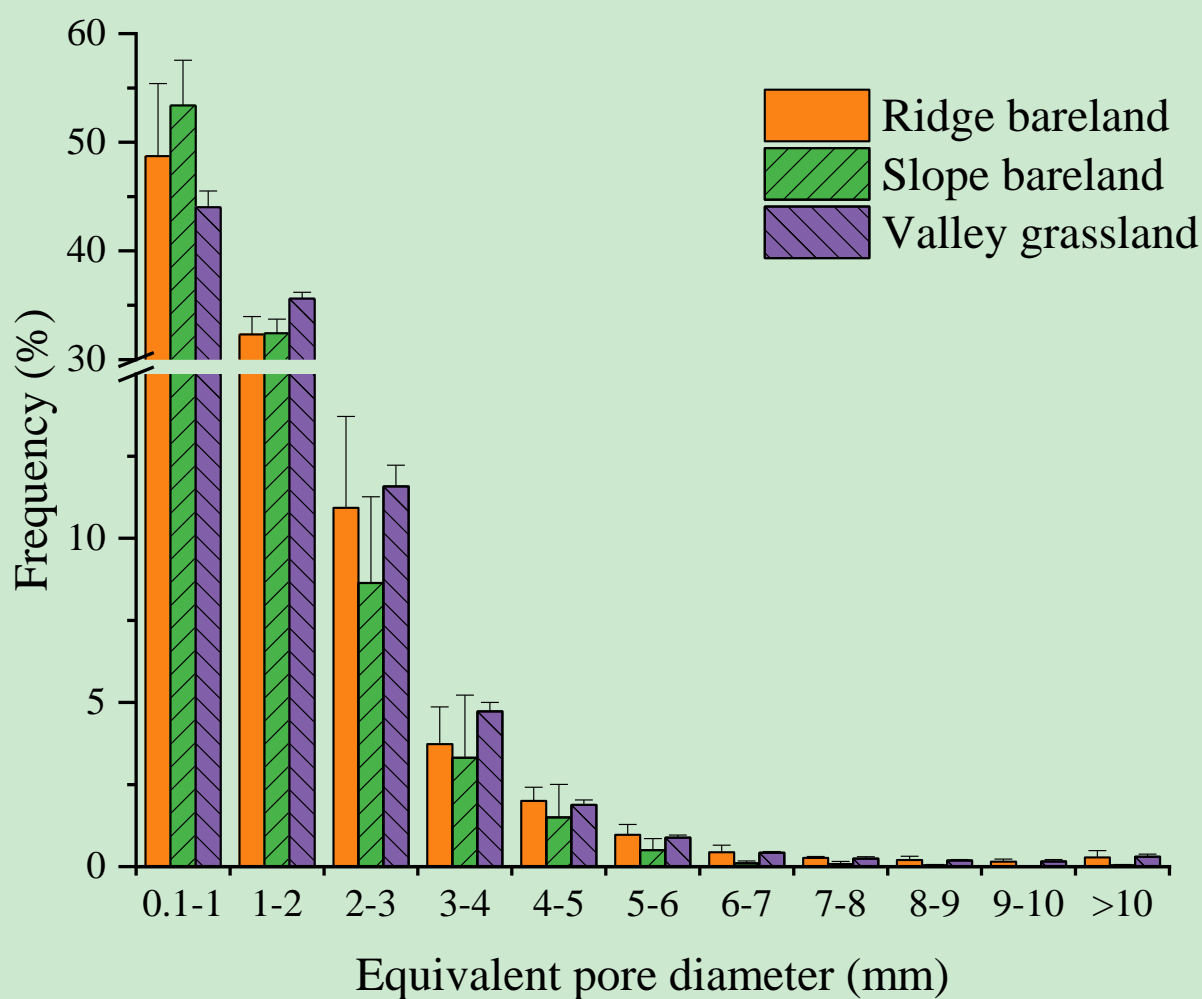


Figure 7 The frequency of equivalent pore diameters of soil columns at different sites.